Crystals **2014**, *4*, 241-261; doi:10.3390/cryst4030241

OPEN ACCESS

crystals

ISSN 2073-4352

www.mdpi.com/journal/crystals

Review

Rare-Earth Calcium Oxyborate Piezoelectric Crystals $ReCa_4O(BO_3)_3$: Growth and Piezoelectric Characterizations

Fapeng Yu [1], Xiulan Duan [1], Shujun Zhang [2,*], Qingming Lu [3] and Xian Zhao [1,*]

1. State Key Laboratory of Crystal Materials and Institute of Crystal Materials, Shandong University, Jinan 250100, Shandong, China; E-Mails: fapengyu@sdu.edu.cn (F.Y.); xlduan@sdu.edu.cn (X.D.)
2. Materials Research Institute, Pennsylvania State University, University Park, PA 16802, USA
3. School of Chemistry and Chemical Engineering, Shandong University, Jinan 250100, Shandong, China; E-Mail: qmlu@sdu.edu.cn

***** Authors to whom correspondence should be addressed; E-Mails: soz1@psu.edu (S.Z.); zhaoxian@icm.sdu.edu.cn (X.Z.); Tel.: +1-814-863-2639 (S.Z.); +86-531-8836-4068 (X.Z.).

Received: 12 April 2014; in revised form: 15 June 2014 / Accepted: 24 June 2014 / Published: 8 July 2014

Abstract: Rare-earth calcium oxyborate crystals, $ReCa_4O(BO_3)_3$ (ReCOB, Re = Er, Y, Gd, Sm, Nd, Pr, and La), are potential piezoelectric materials for ultrahigh temperature sensor applications, due to their high electrical resistivity at elevated temperature, high piezoelectric sensitivity and temperature stability. In this paper, different techniques for ReCOB single-crystal growth are introduced, including the Bridgman and Czochralski pulling methods. Crystal orientations and the relationships between the crystallographic and physical axes of the monoclinic ReCOB crystals are discussed. The procedures for dielectric, elastic, electromechanical and piezoelectric property characterization, taking advantage of the impedance method, are presented. In addition, the maximum piezoelectric coefficients for different piezoelectric vibration modes are explored, and the optimized crystal cuts free of piezoelectric cross-talk are obtained by rotation calculations.

Keywords: ReCOB crystals; crystal growth; dielectric; piezoelectric; sensor

1. Introduction

High temperature sensors are desirable in aerospace and automotive industries for monitoring component conditions to optimize the propulsion system, with operations at temperatures up to 1000 °C, to enable safer, more fuel-efficient and more reliable vehicles; in addition, they are important for nondestructive *in situ* inspection of the structure health of the furnace component or systems in electric generation plants, to improve the safety and reduce life-cycle costs. Compared with the commercial strain gauge and optical fiber sensors, *etc.*, piezoelectric sensors have greater potentials in realizing high temperature (>600 °C) sensing with the merits of high accuracy, fast response time and ease of integration [1–4].

Of all the investigated high temperature piezoelectric materials up to date, crystals in trigonal, tetragonal and monoclinic systems have been extensively investigated. Among these materials, the trigonal lithium niobate ($LiNbO_3$, LN) crystals with *3m* symmetry were reported to possess high piezoelectric coefficient, being on the order of 6–70 pC/N at room temperature, approximately 3–30 times that of commercial α-quartz (SiO_2) (2–3 pC/N). However, the maximum operating temperature of LN-based piezoelectric devices, restricted by their low electrical resistivity (a requirement of $>10^6$ Ohm cm was proposed for comparison, where the materials with low resistivity yet can be used for high frequency applications [1]) at elevated temperature is limited to <600 °C, though the Curie temperature is above 1150 °C [5]. Other important trigonal piezoelectric crystals include the langasite family with the general formula of $A_3BC_3D_2O_{14}$ [6–12] and gallium orthophosphate $GaPO_4$, in the point group of *32* [13–19], these crystals were reported to show modest piezoelectric coefficients (5–7 pC/N) and high melting points (1300–1500 °C for langasite family crystals and ~1670 °C for $GaPO_4$), prior to which, there are no phase transitions observed for langasite family crystals (the phase transition for $GaPO_4$ is about 970 °C). However, the costly component Ga_2O_3 restricted their further implements. The newly developed $Ca_3TaAl_3Si_2O_{14}$ (CTAS) crystals, substituting the Ga with Al elements, were found to possess improved higher temperature properties than $La_3Ga_5SiO_{14}$ (LGS) and to significantly decrease the cost of raw materials; nevertheless, the crystal quality needs to be improved, due to the core defect observed inside the crystals [12]. The tetragonal melilite crystals (point group $\bar{4}2m$, such as $SrLaGa_3O_7$ (SLG), $Ca_2Al_2SiO_7$ (CAS), *etc.*) and fresnoite crystals (point group *4mm*, such as $Ba_2TiSi_2O_8$) were investigated for piezoelectric applications. These crystals show the merits of high melting points (1400–1700 °C) and high effective piezoelectric coefficients d_{eff} (5–18 pC/N) [20–26]; the evaluations of the temperature dependence of dielectric, piezoelectric and electromechanical properties, however, are limited. Of particular significance is that the monoclinic rare-earth calcium oxyborate crystals ($ReCa_4O(BO_3)_3$, ReCOB, Re: rare earth), which have been extensively investigated for nonlinear optical applications in the last two decades [27–33], were reported to exhibit good piezoelectric properties and high electrical resistivity at an elevated temperature of 1000 °C, with no phase transition prior to their melting points (~1400–1520 °C) [1–3,34–38].

Table 1 summarizes the basic characteristics of various high temperature piezoelectric crystals in monoclinic, trigonal and tetragonal systems, where the monoclinic ReCOB crystals were found to exhibit relatively high melting points, as well as relatively large piezoelectric coefficients, promising high temperature piezoelectric sensor applications.

In this review article, crystal growth, dielectric, elastic and piezoelectric property characterizations of the monoclinic ReCOB crystals are surveyed. Different crystal growth techniques, including the Bridgman and Czochralski (Cz) pulling methods, are discussed in Section 2. The crystal orientation related to the physical axes and crystallographic axes for electro-elastic property investigations is studied in Section 3. In Section 4, characterizations of the dielectric, elastic and piezoelectric properties of ReCOB crystals are reviewed. In Section 5, the maximum piezoelectric coefficients for different crystal cuts and the optimized crystal cuts free of cross-talk are discussed. Finally, the significance and challenges of ReCOB crystals are summarized; future research is proposed in Section 6.

Table 1. A comparison of different high temperature piezoelectric crystals. LGS, $La_3Ga_5SiO_{14}$; CTGS, $Ca_3TaGa_3Si_2O_{14}$; CTAS, $Ca_3TaAl_3Si_2O_{14}$; SLG, $SrLaGa_3O_7$; CAS, $Ca_2Al_2SiO_7$; BTS, $Ba_2TiSi_2O_8$; ReCOB, $ReCa_4O(BO_3)_3$.

Symmetry	Crystals	Growth Method	T_c/T_m (℃)	d_{eff} (pC/N)
Trigonal	LGS	Cz	1430 [39]	6~7
	CTGS	Cz	~1370 [40]	~10
	CTAS	Cz	–	~5
	$GaPO_4$	Flux/hydrothermal	970 [41] #	~5
	LN	Cz	1150	~70 [42]
Tetragonal	SLG	Cz	~1650 [43]	~14 [44]
	CAS	Cz	1500	~6 [22]
	BTS	Cz	1445	~18 [23]
Monoclinic	ReCOB	Cz/Bridgman	1400~1520 [1]	~15

Notes: Cz, Czochralski pulling method; # α–β phase transition temperature.

2. Crystal Growth

2.1. Polycrystalline Preparation

The ReCOB polycrystalline materials were prepared by high purity (99.99%) $CaCO_3$, Re_2O_3 (Pr_6O_{11}) and H_3BO_3 powders. They were weighed according to their nominal compositions. Considering the evaporation of B_2O_3 during crystal growth, an excess of H_3BO_3 (1–3 wt%) was added to the starting components, which will benefit the crystal growth [38,45,46]. The starting materials were mixed completely, followed by the calcination ~1000 ℃ for 5–10 h to decompose the H_3BO_3 and $CaCO_3$, after which, the calcined powders were ground, remixed and then pressed into tablets to fabricate ReCOB polycrystalline components at 1100–1200 ℃ for 10–20 h; the solid state reaction follows the equation below:

$$Re_2O_3 + 6H_3BO_3 + 8CaCO_3 = 2ReCa_4O(BO_3)_3 + 8CO_2\uparrow + 9H_2O\uparrow \quad (1)$$

2.2. Approaches for ReCOB Crystal Growth

Different techniques have been applied for ReCOB crystal growth, including the high temperature flux, Bridgman and Cz approaches [47–49]. At the early stage of ReCOB crystal studies, the high temperature flux method was adopted for the crystal growth, where the selection of appropriate flux agent (high temperature solvent) is vital, especially for the crystals with incongruent features. Among ReCOB crystals (except CeCOB and YbCOB), ErCOB, YCOB, GdCOB, SmCOB, NdCOB, PrCOB and LaCOB are congruent melting compounds, while TbCOB and TmCOB were found to possess a very narrow congruent region. Lead oxide was firstly selected as the flux agent for ReCOB crystal growth, with limited success, where the grown crystals were at centimeter scale [47]. Later, the Bridgman and Cz methods, which are favorable for growing crystals with congruent melting features, were utilized. In the following, the growth of ReCOB crystals by the Bridgman and Cz methods is introduced.

2.2.1. Bridgman Method

The Bridgman method, which is also called the Bridgman-Stockbarger method, involves heating polycrystalline materials in a platinum or iridium crucible above its melting point and slowly cooling it from one end, where an oriented seed crystal is located. The crucible is translated from the high temperature region to the low temperature region at a special designed speed; the single crystal is progressively formed along the length of the crucible. Figure 1 shows a schematic set-up of the Bridgman growth system.

Figure 1. Schematic set-up of the Bridgman growth system.

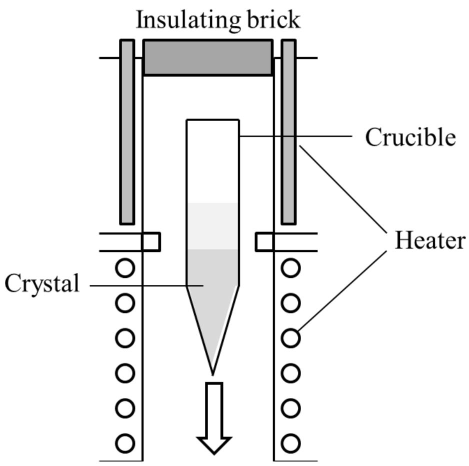

By the Bridgman method [50], the feed materials were prepared by thoroughly mixing the stoichiometric oxides, which were charged into a cylindrical platinum crucible. The material was heated to about 50 ℃ above its melting point, maintained for more than 10 h to make a homogeneous melt. The seeding process (along the <010> or <001> orientation) was performed by adjusting the crucible position and furnace temperature gradient, so that only the top part of the seed was melted. Growth was then driven by lowering the crucible at a rate of 0.2–0.6 mm/h, and the temperature gradient near the solid/liquid interface was normally kept at 30–50 ℃/cm. Recently, large YCOB crystals with a diameter up to 3–4 inches have been reported, using the modified Bridgman furnace [48].

2.2.2. Cz Pulling Method

Cz method is named after Polish scientist, Jan Czochralski, who invented this method in 1916. In the Cz pulling technique, iridium, platinum, molybdenum and graphite crucibles are generally selected and heated in a low–medium radio-frequency furnace. Particularly, for ReCOB crystal growth, an iridium crucible is mostly utilized, due to its high melting point (~2450 ℃) and chemical inertia to the raw materials. Figure 2 gives the schematic set-up of the Cz pulling system.

YCOB and GdCOB single crystals have been grown by the Cz method [27,33,49]. ReCOB materials were melted and kept 30–80 ℃ above their respective melting points for more than 10 h to ensure the homogeneity of the melts. A <010>-oriented crystal seed was selected for the growth, which will benefit the large diameter crystals. The pulling speed was controlled at 0.4–2.0 mm/h, and the rotation speed was varied from 10 to 30 rpm during the crystal growth. When the growth was finished, the crystal was cooled down to room temperature at a low rate of 10–50 ℃/h, to avoid the crystal cracks induced by inner thermal stress. Figure 3 shows the large YCOB single crystals grown by the Cz method (Figure 3a,c) and the Bridgman method (Figure 3b) with a diameter being on the order of 3–4 inches. The obtained crystals were reported to possess X-ray diffraction with a very low full-width at half maximum (FWHM) (~30″) [51] and high optical homogeneity (10^{-6}) [52], exhibiting high crystal quality.

Figure 2. Schematic set-up of the Cz method for crystal growth.

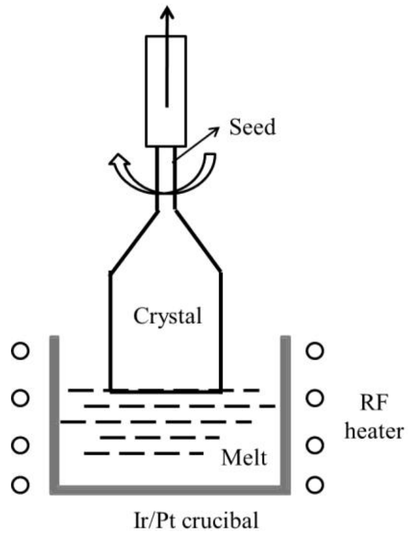

Figure 3. Large YCOB single crystals grown by the Cz method and the Bridgeman method (crystal (**a**) was grown by Crystal Photonics Inc. using Cz method, reprinted with permission from [53]. Copyright 2006 Elsevier; Crystal (**b**) was grown using Bridgeman method, reprinted with permission from [48]. Copyright 2013 Elsevier; and crystals (**c**) were grown using Cz method, reprinted with permission from [46]. Copyright 2013 Chinese Ceramic Society.

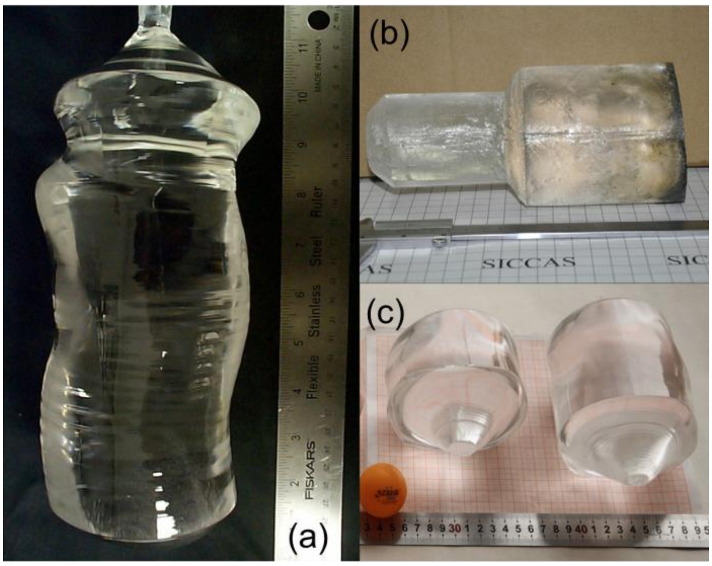

3. Orientation of Monoclinic ReCOB Crystals

ReCOB are monoclinic biaxial crystals belonging to the point group *m*. Therefore, three different orientation systems exist due to the crystal symmetry, including the crystallographic, optical and physical systems. For piezoelectric characterizations, the relationship between the crystallographic and physical axes should be determined, where the physical *Y*-axis is parallel to the crystallographic *b*-axis, *Z*- to the *c*-axis, and the *X*-axis is perpendicular to the *Y* and *Z* axes to form a right-hand orthogonal system according to the IEEE Standard on Piezoelectricity [54], as shown in Figure 4.

The initial orientation step is to verify the (010), ($\bar{2}01$) an (101) faces using X-ray analysis, possessing relatively strong diffraction peaks, from which, the crystallographic axes, *a*, *b* and *c*, can be determined according to the relationships between the interfacial angle and crystallographic plane. Then, the physical axes can be easily determined based on the IEEE standards. Taking YCOB crystals, for example, the angle between the *Z*-axis and (101) face was calculated to be around 57.1°, while the angle between the *X*-axis and ($\bar{2}01$) face was close to 34.6°(Figure 4). It is noteworthy that these angles (interfacial angles, *etc.*) are varied for different ReCOB crystals, due to their different lattice parameters (Table 2). After the orientation of the *X*, *Y* and *Z* axes, the positive *X* and positive *Z* axes can be further confirmed by using a quasi-static piezoelectric d_{33} meter, according to the IEEE Standard on Piezoelectricity [54].

Figure 4. Schematic of the cross-section of Cz-grown YCOB crystals, with the relationship of the crystallographic and physical axes.

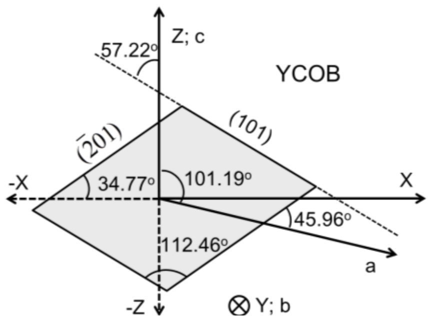

Table 2. Unit cell parameters and interfacial angles for different ReCOB crystals in space group C_m.

Crystals		TmCOB	ErCOB	YCOB	TbCOB	GdCOB	SmCOB	NdCOB	PrCOB	LaCOB
Parameters (Å/Å^3/°) *	*a*	8.068	8.075	8.078	8.072	8.104	8.114	8.145	8.177	8.173
	b	16.01	16.01	16.02	16.00	16.03	16.06	16.07	16.16	16.09
	c	3.522	3.530	3.534	3.545	3.558	3.579	3.607	3.629	3.627
	β	101.11	101.43	101.19	101.25	101.25	101.38	101.37	101.40	101.40
	V	446.56	447.25	448.01	449.06	453.38	457.24	462.81	469.95	467.41
Formula weight *		521.33	519.74	441.65	511.33	509.99	502.78	496.98	493.33	491.68
$\angle 1$ (°) #		112.59	112.45	112.46	112.41	112.26	111.99	111.78	111.66	111.62
$\angle 2$ (°) #		34.74	34.70	34.77	34.75	34.85	34.94	35.08	35.14	35.14
$\angle 3$ (°) #		45.85	46.13	45.96	46.00	46.10	46.32	46.45	46.54	46.57

* PDF #: 00-050-0403 (YCOB); 01-077-0951 (GdCOB); 01-079-1378 (SmCOB); 00-050-0399 (NdCOB); 01-070-7385 (LaCOB); TmCOB [55]; TbCOB [56]; PrCOB [38]; # $\angle 1$: the interfacial angle between (101) and ($\bar{2}01$); $\angle 2$: the interfacial angle between ($\bar{2}01$) and the *X*-axis; $\angle 3$: the interfacial angle between ($\bar{2}01$) and (001).

4. Electro-Elastic Material Constants Determination

Due to the crystal symmetry, there are two different sets of electro-elastic component matrix for monoclinic crystal, relating to point group *m* and point group *2*. The piezoelectric crystals in point group *2* possess eight independent piezoelectric strain coefficients d_{ij}, while crystals in point group *m* exhibit ten independent piezoelectric strain coefficients d_{ij}, four dielectric permittivities ε_{ij} and thirteen elastic compliances s_{ij}. The electro-elastic component matrix for piezoelectric crystals in point group *m* can be written as:

$$\varepsilon_{ij}=\begin{pmatrix}\varepsilon_{11} & 0 & \varepsilon_{13}\\ 0 & \varepsilon_{22} & 0\\ \varepsilon_{13} & 0 & \varepsilon_{33}\end{pmatrix}$$

$$d_{ij}=\begin{pmatrix}d_{11} & d_{12} & d_{13} & 0 & d_{15} & 0\\ 0 & 0 & 0 & d_{24} & 0 & d_{26}\\ d_{31} & d_{32} & d_{33} & 0 & d_{35} & 0\end{pmatrix} \tag{2}$$

$$s_{ij}=\begin{pmatrix}s_{11} & s_{12} & s_{13} & 0 & s_{15} & 0\\ s_{12} & s_{22} & s_{23} & 0 & s_{25} & 0\\ s_{13} & s_{23} & s_{33} & 0 & s_{35} & 0\\ 0 & 0 & 0 & s_{44} & 0 & s_{46}\\ s_{15} & s_{25} & s_{35} & 0 & s_{55} & 0\\ 0 & 0 & 0 & s_{46} & 0 & s_{66}\end{pmatrix}$$

Taking advantage of the impedance method based on the IEEE standard, all of the electro-elastic parameters for ReCOB crystals can be determined. Meanwhile, the elastic stiffness c_{ij} and piezoelectric stress coefficient e_{ij} can be obtained based on the determined elastic compliance s_{ij} and piezoelectric strain coefficient d_{ij}, following the equations below:

$$c=1/s \tag{3}$$

$$e=dc \tag{4}$$

Based on the IEEE standard [54], the dielectric permittivities ε_{ii} (i = 1, 2 and 3) can be evaluated by measuring the capacitance of *X*-, *Y*- and *Z*-cut square plates, respectively. Piezoelectric d_{11} and d_{33} can be obtained by measuring the longitudinal vibration mode of the *X* and *Z* rods, while elastic compliances s_{ii} (i = 1–6) can be calculated from the extensional and shear vibration modes, relating to the piezoelectric coefficient d_{12}, d_{13}, d_{15}, d_{24}, d_{26}, d_{31}, d_{32}, d_{33} and d_{35}. On the contrary, the dielectric cross permittivity ε_{13} and elastic cross compliances s_{ij} ($i \neq j$; i, j = 1–6) can be evaluated by employing oblique crystal cuts that do not lie along or normal to any of the three physical axes. Figure 5 presents different crystal cuts designed for the electro-elastic parameter determination, including the dielectric permittivities, elastic compliances and piezoelectric coefficients. The aspect ratios of the samples (*X*-, *Y*- and *Z*-square plates) for dielectric measurement ranged from 1:8:8 to 1:10:10, whereas for elastic measurement, rectangular samples were used with aspect ratios, *t* (thickness):*w* (width):*l* (length), ranging from 1:2:10 to 1:3:15 and an orientation accuracy <30″. For each crystal cut, 3–5 pieces of samples were prepared for parameter determination.

Figure 5. Crystal cuts for electro-elastic parameter determination ((*a*) *X* rod; (*b*) *Z* rod; (*c*) *XZ* plate; (*d*) *XY* plate; (*e*) *ZY* plate; (*f*) *ZX* plate; (*g*) (*XZw*)45°; (*h*) (*XZw*)30°; (*i*) (*XZw*)−45°; (*j*) *Z*-square plate; (*k*) *X*-square plate; (*l*) *Y*-square plate; (*m*) (*XYt*)45°; (*n*) (*ZXt*)45°; (*o*) (*YZtw*) 45°/−45°).

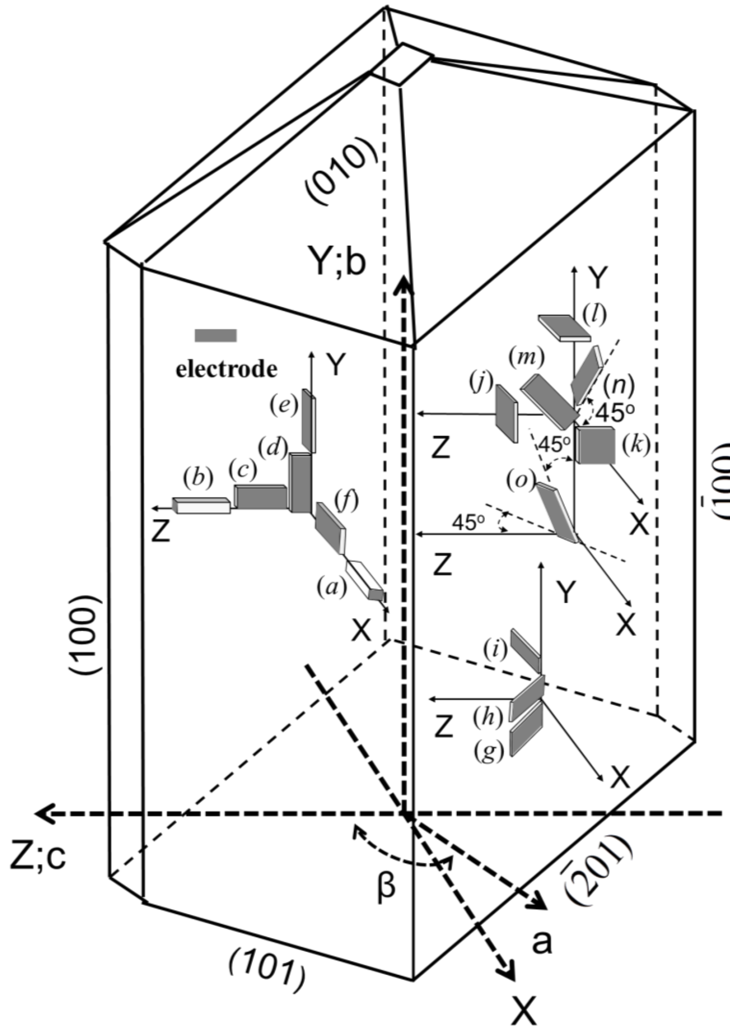

4.1. Dielectric Permittivity

ReCOB crystals possess four independent dielectric permittivities, where the dielectric permittivities ε_{11}, ε_{22}, ε_{33} can be determined from *X*-, *Y*-, and *Z*-cut samples (*k*, *l* and *j*), while for the determination of ε_{13}, sample (*g*) was used (Table 3), following the formulae below:

$$\varepsilon_{11,22,33} = \frac{C_{11,22,33} \cdot t}{A} \tag{5}$$

$$\varepsilon_{33}^{'} = \varepsilon_{11} \sin^2 \theta + 2\varepsilon_{13} \sin\theta \cos\theta + \varepsilon_{33} \cos^2 \theta \tag{6}$$

where *C* is the capacitance of the crystal sample measured at 100 kHz, *t* is the thickness, *A* is the area of the measured plate and $\varepsilon_{33}^{'}$ is the dielectric permittivity for the *Z′*-axis.

Table 3. A summary of different crystal cuts for material constants' determination, reprinted with permission from [57]. Copyright 2014 Wiley-VCH.

Crystal Cuts	Modes	Material constants
X rod (*a*) *Z* rod (*b*)	longitudinal extension	d_{11} d_{33}
ZX plate (*f*) *XY* plate (*d*) *ZY* plate (*e*) *XZ* plate (*c*)	transverse extension	s_{11}, d_{31}, s_{22}, d_{12}, d_{32}, s_{33}, d_{13}
XZ plate (*c*) *ZX* plate (*f*) (*XZw*)45°(*g*)	width shear *	s_{44}, d_{24} s_{66}, d_{26} s_{46}
XZ plate (*c*) *ZX* plate (*f*)	thickness shear	s_{55}, d_{15}, d_{35}
(*XZw*)45°(*g*) (*XZw*)30°(*h*) (*XZw*)−30°(*i*)	transverse extension	s_{13}, s_{15}, s_{35}
(*XYt*)45°(*m*) (*ZXt*)45°(*n*) (*YZtw*)45°/−45°(*o*)	transverse extension	s_{12}, s_{23}, s_{25}
X cut (*k*) *Y* cut (*l*) *Z* cut (*j*) (*XZw*)45°(*g*)	–	ε_{11}, ε_{22}, ε_{33}, ε_{13}

* d_{24} (d_{223}) and d_{26} (d_{212}) are thickness shear vibration modes; however, *XZ* and *ZX* cut samples with electrodes on the *Y* faces were used to determine their values, due to the achievable clean d_{24}/d_{26} vibration modes using the impedance method.

4.2. Piezoelectric Coefficients and Elastic Compliances

For determining the complete set of elastic compliances, piezoelectric coefficients, as well as electromechanical coupling factors, crystal cuts with different orientations were designed, as given in Figure 5. In addition, different crystal cuts with corresponding piezoelectric vibration modes and electro-elastic parameters are summarized in Table 3.

4.2.1. Piezoelectric Coefficients d_{11} and d_{33}

Piezoelectric coefficients d_{11}, d_{33} and elastic compliances s_{11} and s_{33} were determined using the longitudinal mode of *X* and *Z* rods (samples (*a*) and (*b*)), relating to the equations below:

$$s^E = \frac{1}{4\rho l^2 f_a^2 (1-k^2)} \tag{7}$$

$$k^2 = \frac{\pi}{2}\frac{f_r}{f_a}\cot\frac{\pi}{2}(\frac{f_r}{f_a}) \tag{8}$$

$$d = k(\varepsilon s)^{1/2} \tag{9}$$

where ρ, f_r, f_a and k are the crystal density, resonance frequency, anti-resonance and electromechanical coupling factor, respectively.

4.2.2. Piezoelectric Coefficients d_{12}, d_{13}, d_{31}, and d_{32}

Using the transverse extensional mode of *XY*, *XZ*, *ZX* and *ZY* crystal cuts (samples (*c*)–(*e*)), piezoelectric coefficients d_{12}, d_{13}, d_{31} and d_{32} and elastic compliances s_{22}, s_{33} and s_{11} were calculated by Equations (9)–(11).

$$s^E = \frac{1}{4\rho l^2 f_r^2} \tag{10}$$

$$\frac{k^2}{1-k^2} = \frac{\pi}{2}\frac{f_a}{f_r}\tan\frac{\pi}{2}(\frac{f_a - f_r}{f_r}) \tag{11}$$

4.2.3. Piezoelectric Coefficients d_{15}, d_{35}, d_{24}, and d_{26}

d_{15}, d_{35}, d_{24} and d_{26} are thickness shear piezoelectric coefficients; thus, *XZ* and *ZX* crystal cuts (samples (*c*) and (*f*)) with electrodes on the *X* and *Z* faces, respectively, were designed for piezoelectric d_{15} and d_{35} and elastic compliance s_{55} evaluation. However, for the piezoelectric d_{24} and d_{26} and elastic compliance s_{44} and s_{66} determinations, *XZ* and *ZX* cut samples with an electrode on the *Y* faces were used (equivalent to *YZ* and *YX* cut samples with an electrode on *Y* faces), due to the fact that clean width shear vibrations can be obtained. The shear piezoelectric coefficients d_{15}, d_{35}, d_{24} and d_{26} and elastic compliances of s_{55}, s_{44} and s_{66} can be determined by using Equations (8), (9), (12) and (13).

$$s^E = \frac{1}{4\rho t^2 f_a^2(1-k^2)} \tag{12}$$

$$s^E = \frac{1}{4\rho w^2 f_a^2(1-k^2)} \tag{13}$$

4.2.4. Elastic Compliances s_{12}, s_{13}, s_{15}, s_{23}, s_{25}, s_{35} and s_{46}

Except the dielectric, piezoelectric and elastic constants above, there are cross-elastic compliances s_{12}, s_{13}, s_{15}, s_{23}, s_{25}, s_{35} and s_{46} remaining unsolved, requiring the oblique crystal cuts. Crystal cuts (*g*–*i*) with transverse extensional modes were employed to determine the elastic compliances s_{13}, s_{15} and s_{35}, based on Equations (10) and (14), while for the compliance s_{23}, s_{12} and s_{25} evaluations, crystal cuts (*m*–*o*) were designed, combining Equations (10) and (15)–(17). Particularly, the elastic compliance s_{46} was obtained using Equations (13) and (18) by measuring the shear vibration mode of sample (*g*).

$$s'_{33}[(XZw)\theta] = s_{11}\sin^4\theta + (2s_{13} + s_{55})\sin^2\theta\cos^2\theta + 2s_{15}\sin^3\theta\cos\theta + s_{33}\cos^4\theta + 2s_{35}\sin\theta\cos^3\theta \tag{14}$$

$$s'_{22}[(XYt)45^{\circ}] = (s_{22} + 2s_{23} + s_{44} + s_{33})/4 \tag{15}$$

$$s'_{11}[(ZXt)45^{\circ}] = (s_{11} + 2s_{12} + s_{66} + s_{22})/4 \tag{16}$$

$$\begin{aligned} s'_{33}[(YZtw)45^{\circ}/-45^{\circ}] = {} & (4s_{22} + s_{11} + s_{33} + 2s_{15} + 2s_{13} + s_{55} + 2s_{35} + 4s_{23} + 4s_{12} \\ & + 4s_{25} + 2s_{44} + 2s_{66} + 4s_{46})/16 \end{aligned} \tag{17}$$

$$s'_{44}[(XZw)45^{\circ}] = s_{44}/2 + s_{46} + s_{66}/2 \tag{18}$$

Utilizing the crystal cuts listed in Table 3, all of the dielectric permittivities and elastic compliances were obtained, and the results are given in Table 4.

Table 4. Dielectric, piezoelectric and elastic constants of ReCOB (Re = Er, Y, Gd, Nd, Pr and La) crystals.

Elastic Compliances s^E_{ij} (pm^2/N)													
Crystals	s_{11}	s_{12}	s_{13}	s_{15}	s_{22}	s_{23}	s_{25}	s_{33}	s_{35}	s_{44}	s_{46}	s_{55}	s_{66}
ErCOB	7.3	–	–	–	6.7	–	–	8.9	–	31.2	–	21.6	16.6
YCOB [a]	7.2	−0.8	−2.47	−0.4	7.0	0.55	0.54	8.9	−0.12	34.5	−0.37	21.0	16.3
YCOB [b]	7.15	−0.35	−2.8	0.74	6.91	−0.68	−0.46	8.79	−1.2	35.0	3.5	23.0	15.0
GdCOB [b]	7.6	−1.2	−3.9	0.4	7.15	−4.6	−1.5	8.94	0.32	28.0	1.7	23.0	18.0
GdCOB [c]	7.6	−0.92	−0.95	−0.99	7.1	−0.92	−14	8.9	−0.33	17.0	14.0	19.0	18.0
GdCOB	7.6	−1.0	−1.0	−0.4	7.3	1.2	2.8	8.9	−0.6	31.7	−0.9	20.0	18.0
NdCOB [d]	8.3	−1.4	−3.7	2.0	7.4	−0.7	1.8	9.4	−0.4	30.9	0.3	22.4	20.5
NdCOB [e]	8.3	−2.0	−3.5	−0.9	7.5	−1.6	0.5	9.4	0.9	34.0	1.0	22.0	20.0
PrCOB	9.0	–	–	–	7.9	–	–	10.4	–	33.9	–	–	18.7
LaCOB [f]	8.82	−1.1	−2.6	1.1	4.78	−1.2	3.4	10.1	−1.3	34.0	1.3	19.0	18.0

Relative Dielectric Permittivities $\varepsilon^T_{ij}/\varepsilon_0$				
Crystals	ε_{11}	ε_{13}	ε_{22}	ε_{33}
ErCOB	9.5	–	11.8	10.0
YCOB [a]	9.65	0.95	11.8	9.55
YCOB [b]	9.57	−0.96	11.4	9.52
GdCOB [b]	10.5	0.8	14.0	10.4
GdCOB [c]	9.03	0.75	12.35	10.25
GdCOB	9.4	0.9	13.3	9.4
NdCOB [d]	9.9	−1.6	15.5	10.2
NdCOB [e]	9.9	−0.8	15.0	10.0
PrCOB	9.8	–	15.3	10.1
LaCOB [b]	9.87	1.2	14.3	9.87
LaCOB [f]	9.87	−1.24	14.9	9.87

Piezoelectric Coefficients d_{ij} (pC/N)										
Crystals	d_{11}	d_{12}	d_{13}	d_{15}	d_{24}	d_{26}	d_{31}	d_{32}	d_{33}	d_{35}
ErCOB	1.7	3.4	−4.3	−1.4	3.9	7.6	−0.7	−2.8	1.5	−5.5
YCOB [a]	1.7	3.9	−4.2	−1.1	4.4	7.9	−0.77	−2.5	1.4	−5.0
YCOB [b]	1.4	3.8	−4.2	−7.2	−2.6	8.0	−0.22	−2.3	0.83	2.2
GdCOB [b]	2.8	4.8	−3.8	−6.9	0.45	11	−0.77	−2.4	2.5	−4
GdCOB [c]	2.4	4.0	−4.5	0.66	−2.8	2.4	−1.1	−2.2	2.0	−2.7
GdCOB	2.4	4.1	−4.7	−2.2	5.1	11.1	−1.1	−2.5	2.0	−3.8
NdCOB [d]	2.7	4.1	−4.8	3.0	4.1	15.0	−1.9	−3.7	2.1	2.3
NdCOB [e]	1.7	3.9	−4.9	–	–	–	−1.4	−2.5	1.5	–
PrCOB	2.5 *	3.9	−5.2	−1.9	3.1	15.8	−1.5	−2.5	2.0 *	3.3
LaCOB	2.4 *	4.7	–	–	4.0	11.8	–	–	2.0 *	–
LaCOB [b]	2.1	3.9	−3.9	–	–	–	−0.55	−2.2	1.5	–
LaCOB [f]	1.28	3.89	−3.89	0.62	6.41	8.73	−0.55	−2.22	1.10	–

Data ([a–f]) were from [57–62]; * measured by a quasi-static d_{33} meter.

4.2.5. Determination of the Sign of the Piezoelectric Coefficients

According to the IEEE standard [54], the longitudinal piezoelectric d_{11} and d_{33} are positive, while the transverse and shear piezoelectric coefficients are either positive or negative. Therefore, more crystal cuts (rotated around physical axes) are desired to discuss the sign of the piezoelectric coefficient d_{ij} ($i \neq j$) for ReCOB crystals. In this subsection, piezoelectric coefficients for YCOB [a] in Table 4 are discussed.

It is noticed that the piezoelectric d_{35} is a function of d_{11}, d_{13}, d_{31}, d_{33} and d_{15} when rotated around the Y-axis, as expressed below:

$$d_{35}^{'} = 2(d_{11} - d_{13})\cos\theta\sin^2\theta + 2(d_{31} - d_{33})\cos^2\theta\sin\theta + (d_{15}\sin\theta + d_{35}\cos\theta)(\cos^2\theta - \sin^2\theta) \quad (19)$$

$$d_{31}^{'} = (d_{11} - d_{35})\sin\theta\cos^2\theta + (d_{33} - d_{15})\sin^2\theta\cos\theta + d_{31}\cos^3\theta + d_{13}\sin^3\theta \quad (20)$$

Figure 6 shows the variation of piezoelectric d_{35} for YCOB crystals as a function of the rotation angle around the Y-axis (curve (a) in Figure 6). For verification, the experimental shear piezoelectric d_{35} values measured from rotated crystal cuts (ZXw)θ (θ = −60°, −30°, 30° and 60°) were plotted and found to be in good agreement with the calculations, from which, the maximum d_{35} value was determined to be on the order of 6.4 pC/N for (ZXw)−55° crystal cuts. In addition, different d_{35} curves plotted by presuming the opposite sign of the related piezoelectric coefficients in Equation (19) were given as curves (b)–(g), where large discrepancies were observed. The consistency between the calculation and measurement of d_{35} values for YCOB crystals indicates the validity of the reported piezoelectric coefficients d_{11}, d_{13}, d_{31}, d_{33}, d_{15} and d_{35}.

Figure 6. Variation of piezoelectric d_{35} as a function of rotation angle around the Y-axis for YCOB crystals ((a) d_{35}, (b) presuming positive d_{15}, (c) presuming positive d_{35}, (d) presuming positive d_{13}, d_{31}, d_{15} and d_{35}, (e) presuming positive d_{13} and d_{31}, (f) presuming negative d_{13} and (g) presuming positive d_{13}, d_{31}, d_{15} and d_{35}). Reprinted with permission from [57]. Copyright 2014 Wiley-VCH.

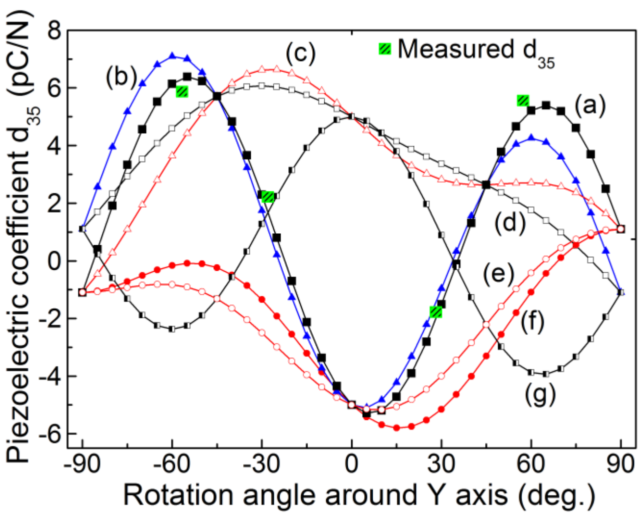

Similarly, the variations of piezoelectric d_{31}, d_{32}, d_{33} and d_{35} for different crystal cuts rotated around the *Y*-axis were plotted and compared in Figure 7, where piezoelectric d_{31} was selected for verifications by measuring the transverse extensional modes of different (*ZXw*)θ crystal cuts (θ = −60°, −45°, −30°, 30° and 60°). The piezoelectric coefficients d'_{31} were determined by Equations (9)–(11), and the results were plotted in Figure 7. It is noted that the measured d'_{31} for different crystal cuts is in good agreement with the calculated results (Equation (20)).

Figure 7. Variations of piezoelectric coefficients d_{31}, d_{32}, d_{33}, and d_{35} as a function of the rotation angle around the *Y*-axis. Reprinted with permission from [57]. Copyright 2014 Wiley-VCH.

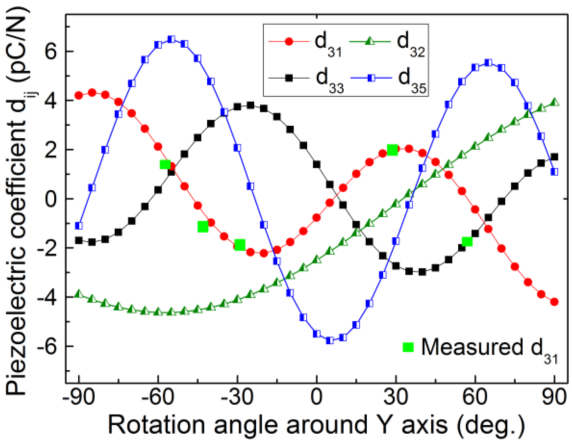

5. The Investigation of Optimum Crystal Cuts

According to the crystal symmetry, ReCOB crystals possess two independent longitudinal piezoelectric coefficients (d_{11} and d_{33}), four transverse piezoelectric coefficients (d_{12}, d_{13}, d_{31} and d_{32}) and four thickness shear piezoelectric coefficients (d_{15}, d_{35}, d_{24} and d_{26}). For piezoelectric sensing applications, various crystal cuts with different piezoelectric vibration modes might be utilized, including the longitudinal (compression) and shear vibration modes, *etc.* Therefore, it is necessary to discuss the optimum crystal cuts with a high piezoelectric coefficient and free of piezoelectric cross-talk.

5.1. Rotated Crystal Cuts with Maximized Values

It is noticed that the maximum values of longitudinal piezoelectric d_{11} and d_{33} for ReCOB crystals should be equal, due to the fact that the *Z* rods (d_{33}) can be obtained by the rotation of *X* rods around the *Y*-axis for −90°, analogous to the thickness shear piezoelectric d_{15} (d_{35}) and d_{26} (d_{24}). Similarly, the transverse piezoelectric d_{12} and d_{13}, d_{31} and d_{32} should be equal from the viewpoint of crystal cut rotation. Equations (21)–(25) reveal the relationships between d_{11} and d_{33}, d_{15} and d_{35}, d_{26} and d_{24}, d_{12} and d_{13} and d_{31} and d_{32}. Evidently, the effective piezoelectric coefficients d'_{11}, d'_{15} and d'_{26} equal to d_{33}, d_{35} and d_{24}, respectively, when rotated around the *Y*-axis for ±90°. Meanwhile, when rotated around the *X*- and *Z*-axes for ±90°, d'_{12} and d'_{31} equal to d_{13} and d_{32}, respectively.

$$d'_{11} = d_{11}\cos^3\theta - d_{33}\sin^3\theta - (d_{31} + d_{15})\sin\theta\cos^2\theta + (d_{13} + d_{35})\sin^2\theta\cos\theta \tag{21}$$

$$d'_{15} = 2(d_{11} - d_{13})\cos^2\theta\sin\theta + 2(d_{33} - d_{31})\sin^2\theta\cos\theta + (d_{15}\cos\theta - d_{35}\sin\theta)(\cos^2\theta - \sin^2\theta) \quad (22)$$

$$d'_{26} = -d_{24}\sin\theta + d_{26}\cos\theta \quad (23)$$

$$d'_{12} = d_{12}\cos^2\theta + d_{13}\sin^2\theta \quad (24)$$

$$d'_{31} = d_{31}\cos^2\theta + d_{32}\sin^2\theta \quad (25)$$

Therefore, the orientation dependence of the longitudinal piezoelectric d_{11}, transverse piezoelectric d_{12} and d_{31} and thickness shear piezoelectric coefficients d_{15} and d_{26} for YCOB crystals were discussed (data refer to YCOB [a] in Table 4). The maximum d_{11} (4.9 pC/N) was obtained from the *X* plate rotated 1° around the *X*-axis and then rotated 52° around the *Z*-axis, whereas the maximum d_{12} and d_{31} were observed for (*XYl*)33° and (*ZXlt*)90°/123°, respectively, being on the order of ~4.6 pC/N. Meanwhile, the highest piezoelectric d_{15} (9.0 pC/N) was obtained for (*XZlt*)90°/60° crystal cuts, and the maximum piezoelectric d_{26} (9.0 pC/N) was achieved in (*YXlt*)180°/30° [(*YXt*)-30°] crystal cut, as reported in [63]. The crystal cuts with maximum d_{11}, d_{12}, d_{31} and d_{15} (the same as d_{26}) values are illustrated in Figure 8a–d, respectively.

For comparison, the maximum values of shear piezoelectric coefficient d_{26} for different ReCOB crystals were studied based on the determined piezoelectric d_{24} and d_{26} values; results are given in Table 5, where PrCOB crystals were found to possess the maximum shear piezoelectric d_{26} value, being on the order of 16.1 pC/N, nearly two times that of ErCOB crystals. The increase of the piezoelectric coefficient for ReCOB crystals was reported to be associated with the difference of the diameter of rare-earth cations (Re^{3+}) and the disorder distribution of Ca^{2+} and Re^{3+} ions in ReCOB crystals [34,47].

Figure 8. The crystal cuts with maximum d_{11}, d_{12}, d_{31} and d_{15} (the same as d_{26}) values for YCOB crystals (**a**) (*XYtw*)1°/52°; (**b**) (*XYl*)33°; (**c**) (*ZXlt*)90°/123°; and (**d**) (*XZlt*)90°/60°, respectively.

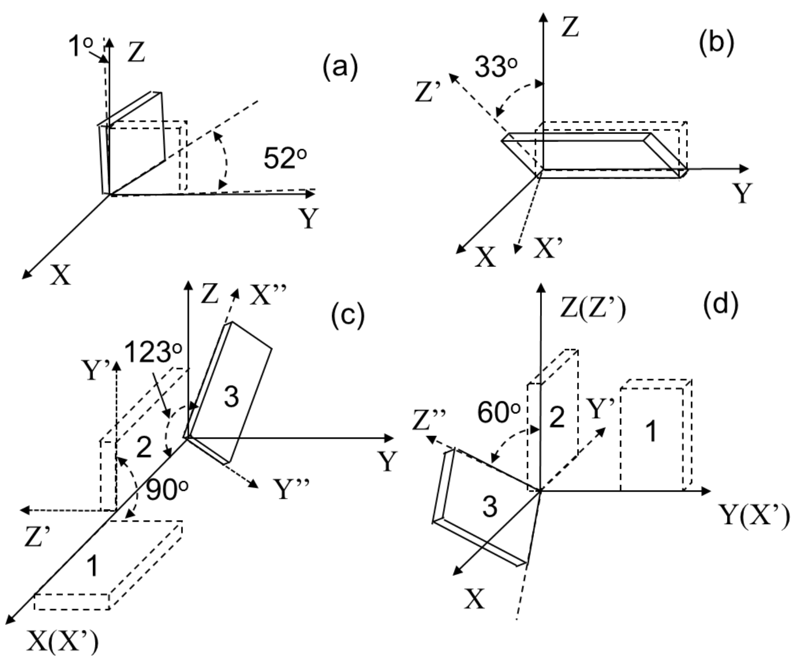

Table 5. Optimum crystal cuts (d_{26} mode) obtained for ReCOB crystals at room temperature.

Crystals	d_{24} (pC/N)	d_{26} (pC/N)	Crystal Cuts	Maximum d_{26} (pC/N)
ErCOB	3.9	7.6	(*YXt*)-25°	~8.5
YCOB	4.4	7.9	(*YXt*)-30°	~9.0
GdCOB	4.7	11.5	(*YXt*)-20°	~12.0
SmCOB	4.1	12.7	(*YXt*)-20°	~13.3
NdCOB	4.1	15.0	(*YXt*)-15°	~15.5
PrCOB	3.1	15.8	(*YXt*)-10°	~16.1
LaCOB	4.0	11.8	(*YXt*)-20°	~12.4

5.2. Rotated Crystal Cuts without Piezoelectric Cross-Talk

For ideal piezoelectric sensors, only the output (charge, current or voltage) is desired when they are loaded (such as force, vibration, pressure or acceleration) along their sensitivity axis; meanwhile, the load normal to that axis should not produce any output. However, real sensors may give an output also to a force normal to their sensitive axis, which may have significant influence on the accuracy of the measuring results, this is called cross-talk (transverse sensitivity) [64]. The cross-talk effect can be weakened or reduced by device structure design; however, minimizing the piezoelectric cross-talk by using the crystal cut design is desirable for improving the accuracy of the sensors. In the following subsection, piezoelectric cross-talk for the longitudinal modes (d_{11}) and thickness shear modes (d_{15} and d_{26}) were discussed, based on the piezoelectric coefficients of YCOB crystals (YCOB [a] in Table 4).

The *X* plates or *X* rods with the first 130° rotation angle around the *Y*-axis and the second 225° rotation angle around the *X*-axis exhibit a relatively good longitudinal piezoelectric response, giving an effective piezoelectric coefficient d_{11} being on the order of ~3.0 pC/N, while other coefficients were found to be −0.8~−1.2 pC/N.

Interestingly, the thickness shear piezoelectric d_{15} and d_{26} were found to possess optimal crystal cuts with negligible piezoelectric cross-talk. Figure 9 presents the variation of piezoelectric coefficients d_{1j} (j = 1–6) for (*XZlw*)45°/θ crystal cuts, where the optimal crystal cut was achieved for (*XZlw*)45°/35°, of which, the shear piezoelectric coefficient d_{15} was determined to be on the order of 8.8 pC/N, with minimized d_{11}, d_{12}, and d_{13} being close to zero, d_{14} and d_{16} < 2.0 pC/N.

Figure 10 gives the variation of piezoelectric coefficients d_{24} and d_{26} as a function of rotation angle around the *Y*-axis, based on the determined piezoelectric coefficients d_{24} (4.4 pC/N) and d_{26} (7.9 pC/N) for YCOB listed in Table 5. It was found that the (*YXt*)330° crystal cut, which equals to the crystal cut (*YXt*)−30°, possess the maximum d_{26} value, being around 9.0 pC/N, with zero piezoelectric d_{24} value, demonstrating free piezoelectric cross-talk. On the contrary, the highest piezoelectric d_{24} (9.0 pC/N) was achieved from the (*YXt*)60° crystal cut, with the d_{26} value being zero. Of particular importance is that these crystal cuts were found to possess the maximum thickness shear piezoelectric coefficients, without the interference from other piezoelectric vibrations, due to the fact that the monoclinic symmetry plane is vertical to the *Y*-axis.

Figure 9. Thickness shear piezoelectric d_{15} for the (*XZlw*)45°/θ crystal cut as a function of rotation angle θ. The inset shows the schematic of the crystal cut (*XZlw*)45°/35°.

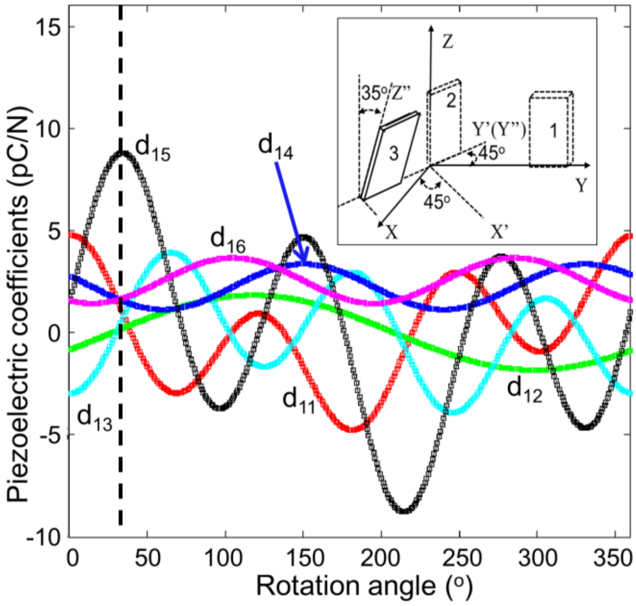

Figure 10. Thickness shear piezoelectric d_{26} for the (*YXt*)θ crystal cut as a function of rotation angle θ. The inset shows the schematic of crystal cut (*YXt*)−30°.

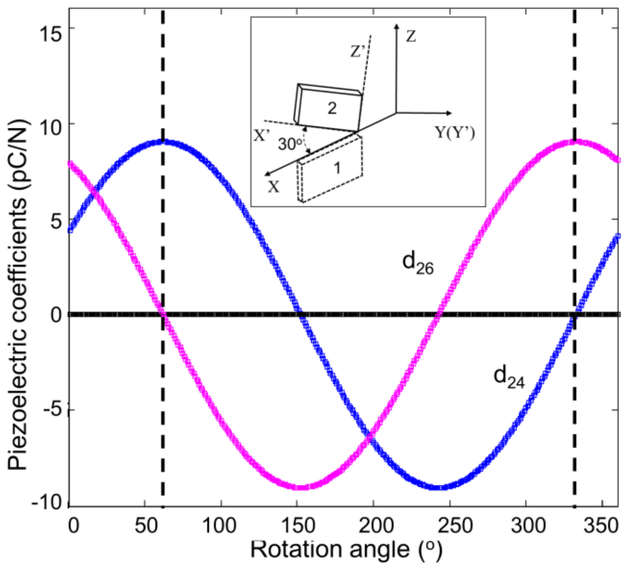

6. Summary and Future Research

6.1. Significance of ReCOB Crystals

The monoclinic ReCOB crystals are promising materials for high temperature piezoelectric sensing. The desirable material merits include the low-cost, reproducible crystals with high quality and large dimension, high piezoelectric coefficient, high electrical resistivity, as well as the high thermal stability of the piezoelectric and electromechanical properties, *etc*. Relevant to this paper, crystal growth and piezoelectric characterization were discussed. Then Bridgman and Cz methods for ReCOB crystal growth were introduced. The relationship between the crystallographic axes and physical axes for ReCOB was discussed for piezoelectric property determination. In addition, procedures for the characterization of the dielectric, elastic and piezoelectric parameters were established, the independent electro-elastic constants were determined, where the highest piezoelectric coefficients d_{26} were achieved, being on the order of 7.6, 7.9, 11.5, 12.7, 15.0, 15.8 and 11.8 pC/N for ErCOB, YCOB, GdCOB, SmCOB, NdCOB, PrCOB and LaCOB, respectively. Of particular significance is that $(YXt)\theta$ crystal cuts not only possess maximum d_{26} coefficients, but also exhibit no cross-talk from other piezoelectric vibrations.

6.2. Future Research

ReCOB piezoelectric crystals are potential materials for high temperature sensor applications. However, several challenges remain for future investigations, including: (1) temperature stability evaluation of the electro-elastic properties, to explore the optimized ReCOB crystals with high thermal stability; (2) structure-property investigation of ReCOB crystals for further improving of the properties at elevated temperatures; and (3) reliability testing of the electro-elastic properties under harsh environments, including high temperature, hard radiation (Gamma and neutron radiations), low oxygen partial pressure, high/low pressure and corrosive/erosive conditions, *etc.*

Acknowledgments

Thomas R. Shrout from Pennsylvania State University is acknowledged for the helpful discussions. Shiyi Guo from Shandong University is thanked for his kind helps during ErCOB crystal growth. Fapeng Yu and Xian Zhao would like to thank the National Natural Science Foundation of China (Grant Nos. 91022034, 51202129, 51372168) and the Natural Science Foundation of Shandong Province (ZR2012EMQ004). This work is also supported by the China postdoctoral Science Foundation (2012M511019).

Author Contributions

Fapeng Yu grew the ReCOB single crystals and evaluated their dielectric and piezoelectric properties. Xiulan Duan studied the crystal structures. Qingming Lu prepared the crystal cuts of different ReCOB crystals for property characterization. Shujun Zhang and Xian Zhao directed this research. Fapeng Yu and Xiulan Duan prepared the manuscript. All the authors contributed to revising the manuscript.

Conflicts of Interest

The authors declare no conflict of interest.

References

1. Zhang, S.J.; Yu, F.P. Piezoelectric materials for high temperature sensors. *J. Am. Ceram. Soc.* **2011**, *94*, 3153–3170.
2. Zhang, S.J.; Jiang, X.N.; Lapsley, M.; Moses, P.; Shrout, T.R. Piezoelectric accelerometers for ultrahigh temperature application. *Appl. Phys. Lett.* **2010**, *96*, doi:10.1063/1.3290251.

3. Zhang, S.J.; Frantz, E.; Xia, R.; Everson, W.; Randi, J.; Snyder, D.W.; Shrout, T.R. Gadolinium calcium oxyborate piezoelectric single crystals for ultrahigh temperature (>1000 °C) applications. *J. Appl. Phys.* **2008**, *104*, doi:10.1063/1.3000560.
4. Jiang, X.N.; Kim, K.; Zhang, S.J.; Johnson, J.; Sakazar, G. High-temperature piezoelectric sensing. *Sensors* **2014**, *14*, 144–169.
5. Shrout, T.R.; Eitel, R.; Randall, R.A. High performance, high temperature perovskite piezoelectric ceramics. In *Piezoelectric Materials in Devices*; EPFL Swiss Federal Institute of Technology: Lausanne, Switzerland, 2002.
6. Fritze, H.; Schneider, O.; She, H.; Tuller, H.L.; Borchardt, G. High temperature bulk acoustic wave properties of langasite. *Phys. Chem. Chem. Phys.* **2003**, *5*, 5207–5214.
7. Zhang, S.J.; Zheng, Y.Q.; Kong, H.K.; Xin, J.; Frantz, E.; Shrout, T.R. Characterization of high temperature piezoelectric crystals with an ordered langasite structure. *J. Appl. Phys.* **2009**, *105*, doi:10.1063/1.3142429.
8. Yu, F.P.; Zhao, X.; Pan, L.H.; Yuan, D.R.; Zhang, S.J. Investigation of zero temperature compensated cuts in langasite-type piezocrystals for high temperature applications. *J. Phys. D Appl. Phys.* **2010**, *43*, doi:10.1088/0022-3727/43/16/165402.
9. Hornsteiner, J.; Born, E.; Riha, E. Langasite for high temperature surface acoustic wave applications. *Phys. Status Solidi A* **1997**, *163*, R3–R4.
10. Sauerwald, J.; Richter, D.; Ansorge, E.; Schmidt, B.; Fritze, H. Langasite based miniaturized functional structures: Preparation, high-temperature properties and applications. *Phys. Status Solidi A* **2011**, *208*, 390–403.
11. Yu, F.P.; Zhang, S.J.; Zhao, X.; Yuan, D.R.; Qin, L.F.; Wang, Q.M.; Shrout, T.R. Investigation of $Ca_3TaGa_3Si_2O_{14}$ piezoelectric crystals for high temperature sensors. *J. Appl. Phys.* **2011**, *109*, doi:10.1063/1.3592347.
12. Xin, J.; Zheng, Y.Q.; Kong, H.K.; Chen, H.; Tu, X.N.; Shi, E.W. Growth of a new ordered langasite structure crystal $Ca_3TaAl_3Si_2O_{14}$. *Cryst. Growth Des.* **2008**, *8*, 2617–2619.
13. Fritze, H. High-temerature bulk acoustic wave sensors. *Meas. Sci. Technol.* **2011**, *22*, doi:10.1088/0957-0233/22/1/012002.
14. Fritze, H. High-temerature piezoelectric crystals and devices. *J. Electroceram.* **2011**, *26*, 122–161.
15. Li, J.; Liang, X.M.; Xu, G.G.; Zhao, H.Y.; Wang, J.Y. Flux growth of $GaPO_4$ crystal. *Piezoelectr. Acoustrooptocs.* **2007**, *29*, 695–696.
16. Philippot, E.; Ibanez, A.; Goiffon, A.; Cochez, M.; Zarka, A.; Capelle, B.; Schwartzel, J.; Détaint, J. A quartz-like material: Gallium phosphate ($GaPO_4$): Crystal growth and characterization. *J. Cryst. Growth* **1993**, *130*, 195–208.
17. Millichamp, J.; Ali, E.; Brandon, N.P.; Brown, R.J.C.; Hodgson, D.; Kalyvas, C.; Manos, G.; Brett, D.J.L. Application of a $GaPO_4$ crystal microbalance for the detection of coke formation in high-temperature reactors and solid oxide fuel cells. *Ind. Eng. Chem. Res.* **2011**, *50*, 8371–8375.
18. Schiopu, P.; Cristea, I.; Grosu, N.; Cracium, A. Development of SAW filters based on $GaPO_4$. In Proceedings of the 2011 IEEE 17th International Symposium for Design and Technology in Electronic Packaging (SIITME), Timisoara, Romania, 20–23 October 2011.
19. Traon, O.L.; Masson, S.; Chartier, C.; Janiaud, D. LGS and $GaPO_4$ piezoelectric crystals: New results. *Solid State Sci.* **2010**, *12*, 318–324.

20. Zhang, Y.Y.; Zhang, H.J.; Yu, H.H.; Sun, S.Q.; Wang, J.Y.; Jiang, M.H. Characterization of disordered melilite Nd:$SrLaGa_3O_7$ crystal. *IEEE J. Quantum Electron.* **2011**, *47*, 1506–1513.
21. Hagiwara, M.; Noguchi, H.; Hoshina, T.; Takeda, H.; Fujihara, S.; Kodama, N.; Tsurumi, T. Growth and characterization of $Ca_2Al_2SiO_7$ piezoelectric single crystals for high temperature sensor applications. *Jpn. J. Appl. Phys.* **2013**, *52*, doi:10.7567/JJAP.52.09KD03.
22. Takeda, H.; Hagiwara, M.; Noguchi, H.; Hoshina, T.; Takahashi, T.; Kodama, N.; Tsurumi, T. Calcium aluminate silicate $Ca_2Al_2SiO_7$ single crystal applicable to piezoelectric sensors at high temperature. *Appl. Phys. Lett.* **2013**, *102*, doi:10.1063/1.4811163.
23. Shen, C.; Wang, J.Y.; Zhang, H.J.; Yin, X.; Zhang, Y.Y.; Xu, H.H.; Han, S.J. Growth and determination of electro-elastic constants of $Ba_2TiSi_2O_8$ crystal. *J. Chin. Ceram. Soc.* **2012**, *40*, 1311–1315.
24. Kimura, M.; Fujino, Y.; Kawanura, T. New piezoelectric crystals: Synthetic fresnoite ($Ba_2Si_2TiO_8$). *Appl. Phys. Lett.* **1976**, *29*, 227–228.
25. Halliyal, A.; Bhalla, A.S.; Markgraf, S.A.; Cross, L.E.; Newnham, R.E. Unusual pyroelectric and piezoelectric properties of fresoite ($Ba_2TiSi_2O_8$) single crystal and polar glass-ceramics. *Ferroelectrics* **1985**, *62*, 27–38.
26. Kimura, M. Elastic and piezoelectric properties of $Ba_2Si_2TiO_8$. *J. Appl. Phys.* **1977**, *48*, 2850–2856.
27. Mockel, R.; Reuther, C.; Gotze, J. REECOB: 20 years of rare earth element calcium oxoborates crystal growth research. *J. Cryst. Growth* **2013**, *371*, 70–76.
28. Furuya, H.; Yoshimura, M.; Kobayashi, T.; Murase, K.; Mori, Y.; Sasaki, T. Crystal growth and characterization of $Gd_xY_{1-x}Ca_4O(BO_3)_3$ crystal. *J. Cryst. Growth* **1999**, *198–199*, 560–563.
29. Zhang, S.J.; Cheng, Z.X.; Lu, J.H.; Li, G.M.; Lu, J.R.; Shao, Z.S.; Chen, H.C. Studies on the effective nonlinear coefficient of $GdCa_4O(BO_3)_3$ crystal. *J. Cryst. Growth* **1999**, *205*, 453–456.
30. Zhang, S.J.; Cheng, Z.X.; Zhang, S.J.; Han, J.R.; Sun, L.K.; Chen, H.C. Growth and noncritical phase-matching third-harmonic-generation of $Gd_xY_{1-x}Ca_4O(BO_3)_3$ crystal. *J. Cryst. Growth* **2000**, *213*, 415–418.
31. Zhang, H.J.; Jiang, H.D.; Wang, J.Y.; Hu, X.B.; Yu, G.W.; Yu, W.T.; Gao, L.; Liu, J.A.; Zhang, S.J.; Jiang, M.H. Growth and characterization of a $LaCa_4O(BO_3)_3$ crystal. *Appl. Phys. A Mater. Sci. Proc.* **2004**, *78*, 889–893.
32. Adams, J.J.; Ebbers, C.A.; Schaffers, K.I.; Payne, S.A. Nonlinear optical properties of $LaCa_4O(BO_3)_3$. *Opt. Lett.* **2001**, *26*, 217–219.
33. Aka, G.; Kahn-Harari, A.; Mougel, F.; Vivien, D.; Salin, F.; Coquelin, P.; Colin, P.; Pelenc, D.; Damelet, J.P. Linear- and nonlinear-optical properties of a new gadolinium calcium oxoborate crystal, $Ca_4GdO(BO_3)_3$. *J. Opt. Soc. Am. B* **1997**, *14*, 2238–2247.
34. Yu, F.P.; Zhang, S.J.; Zhao, X.; Guo, S.Y.; Duan, X.L.; Yuan, D.R.; Shrout, T.R. Investigation of the dielectric and piezoelectric properties of $ReCa_4O(BO_3)_3$ crystals. *J. Phys. D Appl. Phys.* **2011**, *44*, doi:10.1088/0022-3727/44/13/135405.
35. Kim, K.; Zhang, S.J.; Huang, W.B.; Yu, F.P.; Jiang, X.N. $YCa_4O(BO_3)_3$ (YCOB) high temperature vibration sensor. *J. Appl. Phys.* **2011**, *109*, doi:10.1063/1.3598115.

36. Sotnikov, A.; Schmidt, H.; Weihnacht, M.; Zhang, S.J.; Shrout, T.R.; Yu, F.P. Elastic constants of $YCa_4O(BO_3)_3$ and $NdCa_4O(BO_3)_3$ single crystals by the pulse-echo ultrasonic method. In Proceedings of the 2012 IEEE International Ultrasonics Symposium (IUS), Dresden, Germany, 7–10 October 2012.
37. Nakao, H.; Nishida, M.; Shikida, T.; Shimizu, H.; Takeda, H.; Shiosaki, T. Growth and SAW properties of rare-earth calcium oxoborate crystals. *J. Alloys Compd.* **2006**, *408–412*, 582–585.
38. Yu, F.P.; Zhang, S.J.; Cheng, X.F.; Duan, X.L.; Ma, T.F.; Zhao, X. Crystal growth, structure and thermal properties of noncentrosymmetric single crystals $PrCa_4O(BO_3)_3$. *CrystEngComm* **2013**, *15*, 5226–5231.
39. Shimamura, K.; Takeda, H.; Kohnp, T.; Fukuda, T. Growth and characterization of lanthanum gallium silicate $La_3Ga_5SiO_{14}$ single crystals for piezoelectric applications. *J. Cryst. Growth* **1997**, *163*, 388–392.
40. Wang, Z.M.; Yuan, D.R.; Cheng, Z.X.; Duan, X.L.; Sun, H.Q.; Shi, X.Z.; Wei, X.C.; Lü, Y.Q.; Xu, D.; Lü, M.K.; *et al*. Growth of a new ordered langasite structure compound $Ca_3TaGa_3Si_2O_{14}$ single crystal. *J. Cryst. Growth* **2003**, *253*, 398–403.
41. Armand, P.; Beaurain, M.; Ruffle, B.; Menaert, B.; Balitsky, D.; Clement, S.; Papet, P. Characterizations of piezoelectric $GaPO_4$ single crystals grown by the flux method. *J. Cryst. Growth* **2008**, *310*, 1455–1459.
42. Warner, A.W.; Onoe, M.; Coquin, G.A. Determine elastic piezoelectric and dielectric properties of class *3m. J. Acoust. Soc. Am.* **1967**, *42*, 1223–1231.
43. Terentiev, A.V.; Prokoshin, P.V.; Yumashev, K.V.; Mikhailov, V.P.; Ryba-Romanowski, W.; Golab, S.; Pisarski, W. Passive mode locking of a Nd^{3+}:$SrLaGa_3O_7$ laser. *Appl. Phys. Lett.* **1995**, *67*, 2442–2444.
44. Zhang, Y.Y.; Yin, X.; Yu, H.H.; Cong, H.J.; Zhang, H.J.; Wang, J.Y.; Boughton, R.I. Growth and piezoelectric properties of melilite ABC_3O_7 crystals. *Cryst. Growth Des.* **2012**, *12*, 622–628.
45. Liu, Y.Q.; Wei, L.; Yu, F.P.; Wang, Z.P.; Zhao, Y.G.; Han, S.; Zhao, X.; Xu, X.G. Crystal growth and efficient second-harmonicgeneration of the monoclinic $LaCa_4O(BO_3)_3$ crystal. *CrystEngComm* **2013**, *15*, 6035–6039.
46. Pan, Z.B.; Zhang, H.J.; Yu, H.H.; Wang, J.Y. Czochralski growth of large aperture YCOB crystal. *J. Chin. Ceram. Soc.* **2013**, *41*, 55–57.
47. Ilyukhin, A.B.; Dzhurinskii, B.F. Crystal structures of binary oxoborates $LnCa_4O(BO_3)_3$ (Ln = Gd, Tb, and Lu) and $Eu_2CaO(BO_3)_2$. *Russ. J. Inorg. Chem.* **1993**, *38*, 917–920.
48. Wu, A.H.; Jiang, L.W.; Qian, G.X.; Zheng, Y.Q.; Xu, J.; Shi, E.W. Bridgman growth of large-aperture yttrium calcium oxyborate crystal. *Mater. Res. Bull.* **2012**, *47*, 2689–2691.
49. Aka, G.; Kahn-Harari, A.; Vivien, D.; Benitez, J.M.; Salin, F.; Godard, J. A new nonlinear and neodymium laser self-frequency doubling crystal with congruent melting $Ca_4GdO(BO_3)_3$, (GdCOB). *Eur. J. Solid State Inorg. Chem.* **1996**, *33*, 723–736.
50. Luo, J.; Fan, S.J.; Xie, H.Q.; Xiao, K.C.; Qian, S.X.; Zhong, Z.W.; Qian, G.X.; Sun, R.Y.; Xu, J.Y. Thermal and nonlinear optical properties of $Ca_4YO(BO_3)_3$. *Cryst. Res. Technol.* **2001**, *36*, 1215–1221.

51. Yu, F.P.; Duan, X.L.; Zhang, S.J.; Yu, Y.G.; Ma, T.F.; Zhao, X. Temperature dependence of electro-elastic properties of yttrium calcium oxyborate single crystals. In Proceedings of the 2012 Symposium on Piezoelectricity, Acoustic Waves and Device Applications, Shanghai, China, 23–25 November 2012.
52. Zheng, Y.Q.; Wu, A.H.; Gao, P.; Tu, X.N.; Liang X.Y.; Hou, J.; Yang L.M.; Wang, T.; Qian, L.J.; Shi, E.W. Laser damage threshold and nonlinear optical properties of large aperture elements of YCOB crystal. In Proceedings of Pacific Rim Laser Damage 2011: Optical Materials for High Power Lasers, Shanghai, China, 12 January 2012.
53. Fei, Y.T.; Chai, B.H.T.; Ebbers, C.A.; Liao, Z.M.; Schaffers, K.I.; Thelin, P. Large-aperture YCOB crystal growth for frequency conversion in the high average power laser system. *J. Cryst. Growth* **2006**, *290*, 301–306.
54. *IEEE Standard on Piezoelectricity*; ANSI/IEEE Standard; IEEE: New York, NY, USA, 1987.
55. Liu, Y.Q.; Yu, F.P.; Wang, Z.P.; Hou, S.; Yang, L.; Xu, X.G.; Zhao, X. Bulk growth and nonlinear optical properties of thulium calcium oxyborate single crystals. *CrystEngComm* **2014**, doi:10.1039/C4CE00869C.
56. Yuan, D.S.; Jia, Z.T.; Wang, J.; Gao, Z.L.; Zhang, J.J.; Fu, X.W.; Shu, J.;Yin Y.R.; Hu, Q.Q.; Tao, X.T. Bulk growth, structure, and characterization of the new monoclinic $TbCa_4O(BO_3)_3$ crystal. *CrystEngComm* **2014**, *16*, 4008–4015.
57. Yu, F.P.; Hou, S.; Zhang, S.J.; Lu, Q.M.; Zhao, X. Electro-elastic properties of $YCa_4O(BO_3)_3$ piezoelectric crystals. *Phys. Status Solidi A* **2014**, *211*, 574–579.
58. Shimizu, H.; Nishida, T.; Takeda, H.; Shiosaki, T. Dielectric, elastic and piezoelectric properties of $RCa_4O(BO_3)_3$ (R = rare-earth elements) crystals with monoclinic structure of point group *m*. *J. Cryst. Growth* **2009**, *311*, 916–920.
59. Pawlaczyk, C.; Markiewiz, E.; Kłos, A.; Hofman, W.; Pajaczkowska, A. Elastic and piezoelectric properties of gadolinium calcium oxoborate $GdCa_4O(BO_3)_3$ crystal. *Phys. Status Solidi A* **2006**, *203*, 2103–2118.
60. Yu, F.P.; Zhang, S.J.; Zhao, X.; Yuan, D.R.; Wang, C.M.; Shrout, T.R. Characterization of neodymium calcium oxyborate piezoelectric crystal with monoclinic phase. *Cryst. Growth Des.* **2010**, *10*, 1871–1877.
61. Karaki, T.; Adachi, M.; Kuniyoshi, Y. Evaluation of material constants in $NdCa_4O(BO_3)_3$ piezoelectric single crystal. *J. Electroceram.* **2008**, *21*, 823–826.
62. Shimizu, H.; Kodama, K.; Takeda, H.; Nishida, T.; Shikida, T.; Okamura, S.; Shiosaki, T. Evaluation of material constants and temperature properties in lanthanum calcium oxoborate $LaCa_4O(BO_3)_3$ single crystals. *Jpn. J. Appl. Phys.* **2004**, *43*, 6716–6720.
63. Yu, F.P.; Zhang, S.J.; Zhao, X.; Yuan, D.R.; Wang, Q.M.; Shrout, T.R. High temperature piezoelectric properties of yttrium calcium oxyborate single crystals. *Phys. Status Solidi R* **2010**, *4*, 103–105.
64. Gautschi, G. *Piezoelectric Sensorics: Force, Strain, Pressure, Acceleration and Acoustic Emission Sensors, Materials and Amplifiers*, 2nd ed.; Springer-Verlag: Berlin, Germany, 2002.